THE PHOTOGRAMMETRIC RECORD

The Photogrammetric Record 32(160): 513–536 (December 2017)
DOI: 10.1111/phor.12225

INTACT ROCK BRIDGE BREAKAGE AND ROCK MASS FRAGMENTATION UPON FAILURE: QUANTIFICATION USING REMOTE SENSING TECHNIQUES

MARGHERITA C. SPREAFICO (margherita.spreafico@unimib.it)
University of Milano-Bicocca, Milan, Italy

FRANCESCA FRANCI* (francesca.franci2@unibo.it)
GABRIELE BITELLI (gabriele.bitelli@unibo.it)
LISA BORGATTI (lisa.borgatti@unibo.it)
University of Bologna, Bologna, Italy

MONICA GHIROTTI (ghrmnc@unife.it)
University of Ferrara, Ferrara, Italy

**Corresponding author*

Abstract

In this work, two processes related to the onset and the evolution of large-scale rockfalls have been analysed by means of remote sensing techniques. First, the number of rock bridges as a proportion of pre-existing fractures has been estimated in a newly formed landslide scarp by analysing the spectral information of the rock mass in terrestrial laser scanner (TLS) and unmanned aerial vehicle (UAV) photogrammetric point clouds. Second, the fragmentation of the rock mass after failure has been assessed by comparing the percentage of newly formed fractures in the scarp and in the deposit. For this purpose, an orthophoto of the landslide deposit was classified using an object-based method. The presented workflow gained new data on the intact rock breakage during and after failure, and consequently deepened knowledge about rock failure and fragmentation mechanisms.

KEYWORDS: fragmentation, object-based classification, rock bridges, spectral information, terrestrial laser scanner, UAV

INTRODUCTION

THE CHARACTERISATION of discontinuity persistence and intact rock bridges is one of the main challenges of rock slope mechanics. Persistence is defined as the areal extent or size of a discontinuity (Cruden, 1977; International Society for Rock Mechanics, 1978; Sturzenegger and Stead, 2009). Rock bridges are intervals of intact rock separating coplanar or non-coplanar discontinuities. Despite their influence on rock mass strength and stability having

© 2017 The Authors
The Photogrammetric Record © 2017 The Remote Sensing and Photogrammetry Society and John Wiley & Sons Ltd

been known for decades (Einstein et al., 1983), their quantification still remains an open issue. Several authors have tried to quantify and incorporate rock bridges in stability analyses; an overview of this topic can be found in Tuckey and Stead (2016). Two methods have been applied in the literature to quantify rock bridges: back analyses through numerical modelling (Fischer et al., 2010; Gischig et al., 2011) and visual mapping of failure surfaces, mostly in cases of small-scale failures.

When performing visual mapping, one of the most evident differences between fresh and pre-existing fractures in a newly formed landslide scarp is the colour of the rock surface, mainly due to the action of physical and chemical weathering processes. Among others, Frayssines and Hantz (2006) discriminated between the light beige to light rosy, or dark grey, fresh intact rock (depending on the rock type) and the white-orange colour of the calcite crust, covering the pre-existing surfaces. They compiled a database of 25 rock falls, finding a correlation between the percentage of rock bridges detected in the scar and the mean thickness of fallen rock slabs. Paronuzzi and Serafini (2009) recognised a wide rock bridge (about 3 m^2) in the scar of a fallen overhanging slab, analysing the different colours of the rock surface in the scarp. Sturzenegger and Stead (2012) recognised irregular, non-planar, fresh rock surfaces and older, weathered joint surfaces in the Palliser (Canada) rockslide by examining photogrammetric 3D models.

Terrestrial laser scanner (TLS) techniques are widely used for landslide mapping, modelling and monitoring (Jaboyedoff et al., 2012). In recent years, unmanned aerial vehicle (UAV) photogrammetry has expanded the close range photogrammetric domain, introducing a low-cost alternative that combines terrestrial and aerial techniques (Eisenbeiss, 2009) in order to create dense, coloured point clouds.

TLS laser intensity and point cloud spectral information can be used to discriminate, classify and filter the data. Even if point cloud classification algorithms are predominantly based on geometric information (such as roof or vegetation extraction), Lichti (2005) presented a TLS point cloud classification method based on multispectral data. Franceschi et al. (2009), Burton et al. (2011) and Penasa et al. (2014) used TLS intensity to classify between different lithologies. Kurz et al. (2012) differentiated limestone from dolomite by analysing hyperspectral images combined with TLS data.

In the present study, a semi-automatic approach is proposed. It is based on the degree of weathering, namely the presence of iron-oxide coatings or staining along fractures, and thus on the different colour of the discontinuities in the rock mass. By analysing the colour of rock surfaces, this research discriminates between discontinuities that were already open before the final collapse, including both pre-existing fracture planes and rock breakage that occurred before the failure (the time needed for weathering of these surfaces to occur) and rock bridge breakage during the final stage of the failure (for example, during the final collapse or a relatively small amount of time prior to it).

Estimation of the proportion (percentage) of rock bridges was performed on coloured TLS and UAV-image point clouds of the failure scar, acquired a few days after the failure. The fragmentation of the rock blocks after failure can occur through: (1) breakage of intact rock; (2) failure along pre-existing discontinuities; and (3) a combination of the previous two. Estimating the amount of fragmentation is not trivial. Ruiz-Carulla et al. (2015) tried to derive it from a comparison of block-size distribution before and after detachment. However, even if boulder size in the deposit can be measured in the field or by photo-analytical techniques (Crosta et al., 2007), a high degree of uncertainty remains concerning the estimation of the block size prior to the failure.

A comparison between the proportion of fresh fractures formed during failure and the ones measured in the landslide deposit, after the impact between falling blocks and/or the

© 2017 The Authors

ground surface, can assist in the determination of the fragmentation that has occurred in the failed rock mass after the detachment phase.

This procedure was applied by means of a supervised object-based classification on an orthophoto of the landslide deposit. This approach, classifying groups of image pixels based on features such as shape and texture, coupled with spectral characteristics, permitted, firstly, mapping of the blocks in the deposit area (Franci and Spreafico, 2016) and, subsequently, assigning their surfaces to different classes representing newly formed or pre-existing fractures. The approach was tested on the scar of the recent San Leo 2014 failure in Italy (Spreafico et al., 2017).

Based on the results, the location and the orientation of the pre-existing fractures in the scar were investigated. The estimated proportion of rock bridges was then compared with the one inferred using numerical modelling techniques.

Case Study

The rock cliff chosen as the case study is situated in the northern Apennines (Italy), on the north-east side of the San Leo plateau. This plateau is composed, from the bottom to the top, of limestones of the San Marino Fm. (formation), mainly outcropping in the northern and eastern cliffs, and sandstones of the Monte Fumaiolo Fm., more visible in the southern and western slopes. The limestone appears to be massive at the bottom of the slab, becoming more thinly stratified and progressively richer in sandy fraction towards the top. The sandstone is mainly characterised by thick, flat, parallel layers composed of thinner cross-bedded sets. The plateau lies on the highly fissured and over-consolidated Argille Varicolori clay-shales. The north-east cliff has been recently affected by a rock topple (27th February 2014), involving of the order of 300 000 m^3 of rock. The landslide debris was spread over an area of about 70 000 m^2 (Fig. 1), reaching the opposite side of the valley and up to 30 m above the valley bottom.

A full description of the event and the interpretation of the landslide mechanisms can be found in Spreafico et al. (2016, 2017). Briefly, undermining of the clay-rich units at the foot of the cliff brought about the failure and toppling over of the outer portions of the plateau. This mechanism was favoured by the presence of pre-existent persistent sub-vertical discontinuities in the rock mass. The failure took place along these pre-existing discontinuities and the breakage of intact rock bridges. In fact, after the 2014 event a well-defined failure surface could be identified at the top of the eastern side of the cliff. This surface, clearly weathered, was recognised as the pre-existing discontinuity along which part of the failure took place (Spreafico et al., 2016). Other open discontinuities, with similar attitude, were recognised on the top of the plateau.

After the failure, due also to the risk posed to a medieval village resting on the top of the plateau, great efforts were expended in collecting topographical data, both as laser scans and as terrestrial and UAV photogrammetric models of the cliff and landslide deposit.

Materials and Methods

The present work focuses on the potential of using the spectral information in the visible part of the electromagnetic spectrum to discriminate between weathered and freshly exposed rock surfaces, and thus to recognise pre-existing discontinuities in the newly formed landslide scarp and deposit. The red/green/blue (RGB) intensities derived from the terrestrial camera, coupled with the TLS and UAV data, were used to discriminate between these two classes. The methodology applied to quantifying the proportion of fresh fractures

© 2017 The Authors

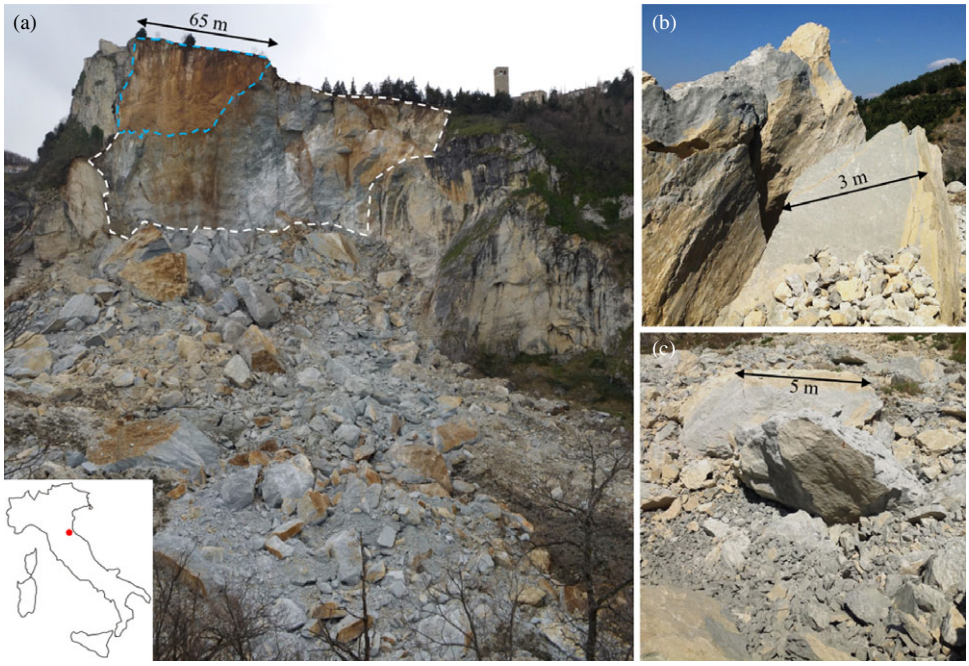

FIG. 1. Photographs of the 2014 San Leo landslide in Italy, acquired a few days after the landslide. (a) The difference in colour between fresh (grey) and weathered (white-orange) fractures can be appreciated in the landslide scarp and in the deposit. The dashed line indicates the boundary of the landslide scarp. The light-blue dashed line highlights the distinct pre-existing surface, identified at the top of the eastern side of the cliff and named SL3.1 in Spreafico et al. (2016). (b), (c) Examples of boulders in the deposit area.

in the cliff consisted of several different phases, starting from the visual inspection of the TLS and UAV point clouds, the selection and analysis of the colour intensities in different test areas, and finally the choice of the best classification rules, based on the RGB intensities and their linear combinations. Other multispectral bands were not available.

An object-based classification was then applied to identify and quantify the percentage of new fractures in the landslide deposit. The difference between the proportion of fresh fractures recognised on the cliff and in the deposit can provide an evaluation about the degree of fragmentation that has occurred during the rebound phase and upon impact. A landslide deposit orthophoto (ground sample distance (GSD) of 5 cm), obtained from the UAV survey, was made available by the Emilia-Romagna Region (Agenzia per la sicurezza territoriale e la protezione civile, Servizio Area Romagna). The adopted methodology is presented in Fig. 2.

Intact Rock Bridge Quantification

Two point clouds of the same area, acquired in different periods and with different techniques (TLS and photogrammetry), were analysed to test the adopted procedure and avoid: (1) artefacts related to light conditions during the image acquisition; (2) effects due to the presence of humidity on the cliff (a laser beam is not reflected by water); and (3) to classical photogrammetric and remote sensing biases, for example, occlusions.

© 2017 The Authors

In particular, a TLS point cloud was acquired on the 6th March 2014, just a few days after the failure, with a Riegl VZ-400 laser scanner, achieving a point density of about 5 cm. Two scan positions were used. The calibrated digital camera, coupled with the laser scanner, permitted the RGB information to be obtained. The coloured point cloud (more than 53 million points) was then georeferenced in the UTM-WGS 84 system by a global navigation satellite system (GNSS) survey. After post-processing, the overall accuracy of the point cloud was sub-centimetre (Riegl VZ-400 datasheet) in terms of relative positioning, and at the centimetre level in terms of absolute orientation. The point cloud deriving from TLS is composed of a set of spatial coordinates with the associated intensity, that is, the power of the backscattered laser signal. Besides this data, RGB images acquired by external or internal digital cameras can be easily used to colour the *X*, *Y*, *Z* point cloud.

Some weeks later (in the second half of March 2014) a UAV photogrammetric survey was executed by SAL Engineering. A calibrated Canon 550D camera, mounted on a hexacopter, was used for the UAV photogrammetric survey. Ground control points (GCPs) were used to georeference each flight. The point cloud was created using a structure-from-motion (SfM) approach. The declared accuracy was 0·08 to 0·15 m in elevation and 0·03 to 0·10 m in planimetry; the point spacing was about 1 to 2 cm (Agenzia per la sicurezza territoriale e la protezione civile, Servizio Area Romagna).

The colour data in both point clouds is expressed in terms of RGB (24 bits). If the investigated cliff can be considered as composed of similar rock units, the colour of their surface can be assumed to depend only on the weathering they underwent. In particular, when rocks containing iron and magnetite are exposed to air and water, their colour tends to change, turning to reddish-brown, due to chemical weathering. The San Leo plateau is formed by San Marino limestones and Monte Fumaiolo sandstones. These two units can be

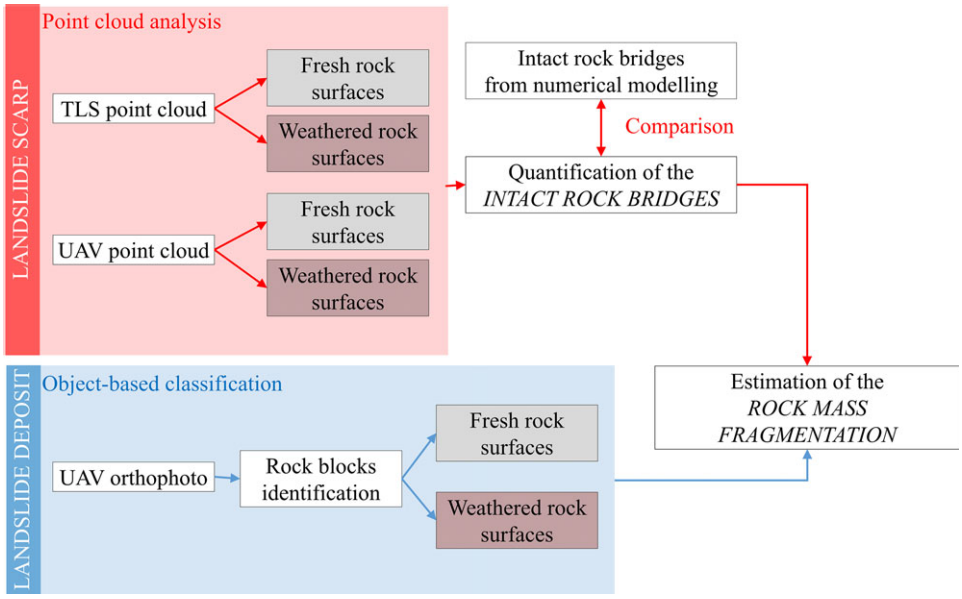

FIG. 2. Flowchart showing the methodology used for the quantification of the intact rock bridges' percentage in the landslide scarp and for the estimation of the rock mass fragmentation amount that occurred after failure.

© 2017 The Authors

considered similar as, on fresh surfaces, they have a relatively uniform light-grey colour. This investigation was mainly interested in the colours of the rock cliff: greyish for the recently formed rock surfaces and brownish for the iron-oxide coatings or staining on pre-existing fractures. The research tried to understand which, among the primary colours (R, G and B) and their linear combinations could be used to discriminate between freshly exposed and weathered rock surfaces. Considering that, according to the additive RGB colour model, the grey colour is the result of triplets in which R = G = B, whereas the brown colour is made by mixing red and green, the blue component can probably be used to discriminate between fresh and weathered surfaces.

The open-source 3D point cloud processing software CloudCompare, version 2.7 (Girardeau-Montaut, 2016), was used to inspect the intensities of the R, G and B colour components in different areas of the point clouds (Fig. 3), allowing the identification of colour combinations which permit a first discrimination between the freshly exposed and weathered surfaces. For each of these combinations some statistical analysis was performed, for example, mean colour intensity in different areas and colour intensity distribution curves, comparing the colour intensity against the number of points. Finally, in order to choose the most meaningful combinations, test areas, representative of the fresh-to-weathered rock-surface ratio, were examined. About 5% of the total number of points in each point cloud were identified for each class (fresh or weathered). Their intensity distribution curves were inspected to understand the main differences between the classes in terms of colour. Where possible, an intensity threshold between the two classes was estimated. Each component (R, G and B) and some linear combinations (such as (R + G + B)/3 or R − B) were tested based on the findings of the visual inspection.

To evaluate the percentage of fresh to pre-existing surfaces, the point clouds were then classified, based on the intensity thresholds: for example, all the points with a colour intensity higher or lower than the threshold were exported, counted and compared with the total number of points.

Possible sources of error can be identified in this evaluation. Depending on the geometry of the scene, not all the parts of the point clouds have the same density (spacing between points). A sub-planar geometry of the point cloud to be analysed can help limit this error. However, the presence of water on the cliff can result in low point-density areas in

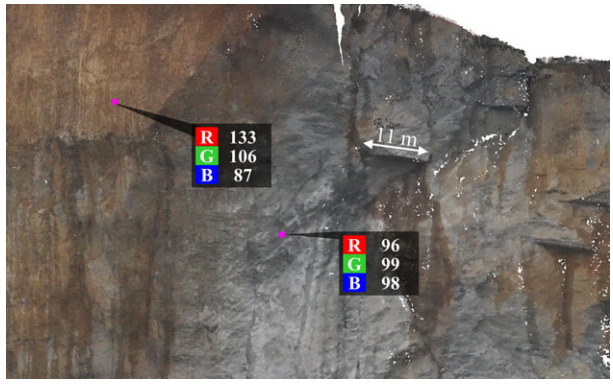

FIG. 3. Example of point cloud inspection: the point on the left is located on a weathered surface, while the one on the right belongs to a fresh fracture. The differences in RGB intensity values can be appreciated.

© 2017 The Authors

TLS point clouds. Furthermore, if more than one scan is joined together to create the final point cloud, the areas in which these scans overlap will have a higher point density. In order to achieve the same point density along the entire cliff, before applying the described procedure the point clouds were resampled based on the minimum space between points. The resulting resampling factor depends on the initial number of points and on the point spacing in the lower density areas. In CloudCompare, the point density is estimated by counting, for each point, the number of neighbours N inside a sphere of radius r; it can be expressed as a volume density, namely, the number of neighbours divided by the neighbourhood volume. Considering a sphere of radius 1 m, the original TLS point cloud had a volume density varying from 0·2 to 641 points/m^3, while after resampling the comparable density is 0·2 to 3·6 points/m^3 (Fig. 4). After this volume density resampling, the point densities of the areas classified as fresh or weathered surfaces were further checked, to ensure a similar point spacing in both classes. Such point cloud resampling is thus suggested if the goal is the quantification of the fresh-to-pre-existing surface percentages. If, instead, the location of the fresh/pre-existing discontinuities has to be investigated in more detail, the original point cloud data would be better to avoid the loss of any information.

The results were validated against visual recognition of weathered discontinuities in selected test areas. Photographs taken the day after the failure were used to aid the visual mapping procedure (Fig. 5). About 20% of the total number of points were manually classified, both on the TLS and the photogrammetric point clouds, and then compared with the results of the illustrated procedure (as outlined in Fig. 2). The visual recognition was based on colour information, fracture orientation and fractography principles (see Tuckey, 2012).

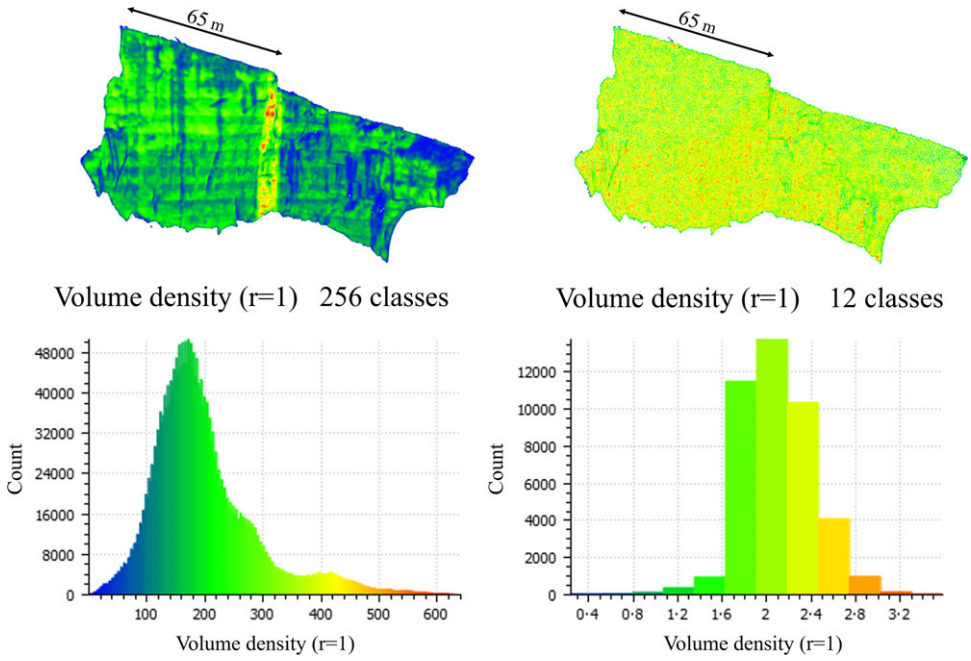

FIG. 4. Point density estimated in CloudCompare for the TLS point cloud before (left) and after (right) the resampling procedure; r refers to the sphere radius used for the calculation.

© 2017 The Authors

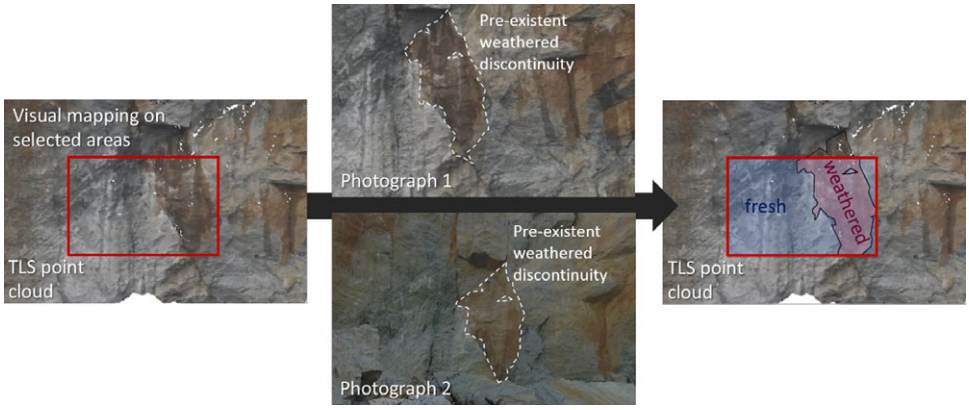

FIG. 5. Example of the visual recognition of weathered discontinuities, used in the result validation phase. The visual mapping was performed in selected areas. The operator was aided by photographs of the failure surface, taken from different viewpoints.

The resulting relative operating characteristic (ROC) curves were used to evaluate which colour component or combination of colours can be used to better estimate the number of pre-existing fractures. ROC curves represent the relationship between sensitivity and specificity of a test over all possible threshold or cut-off values (Beck and Shultz, 1986; Cervi et al., 2010; Hajian-Tilaki, 2013; Pontius and Parmentier, 2014). The specificity represents the threshold chosen to discriminate between fresh and pre-existing surfaces. In each classification, for different threshold values, four classes can be obtained: true negative, true positive, false negative and false positive. The ROC plot can be obtained by graphing the true and false positive rates at different threshold settings. The number of points correctly classified as a proportion of the total (the sensitivity of the model) is thus plotted against the specificity. An estimate of the global accuracy of the model can be obtained by analysing the area under the curve (AUC). In the present work, ROC curves relate only to selected areas where both manual and the semi-automatic classifications were applied.

The percentage of intact rock bridges resulting from the best classification for the two point clouds was then compared with the one estimated by a numerical modelling back analysis of a section of the same cliff (Spreafico et al., 2017). Furthermore, the orientation and the location of pre-existing discontinuities were investigated by comparing the results obtained with discontinuity orientation analysis.

Rock Mass Fragmentation

After the detachment and free-fall phases of a rockfall, rock boulders tend to fragment into smaller blocks due to impact with others blocks and/or with the ground. This process is influenced by various factors, among which are: (1) the fall height; (2) the energy of the impact; (3) slope materials; (4) mechanical properties of the falling rock blocks; (5) the land cover; and (6) the dimensions of the blocks.

This paper presents a new methodology to estimate the degree of fragmentation. A supervised object-based classification procedure was performed on the orthophoto of the landslide deposit in order to first detect the blocks and then to distinguish, on their sides, weathered pre-existing surfaces and fresh fractures. The resulting total percentage of fresh fractures was then compared with that estimated from the analysis of the scarp surface. The

© 2017 The Authors

difference between the two should represent the new fracturing produced during the rockfall event. Using the orthophoto only a part of the deposit can be investigated, as buried blocks and block surfaces with unfavourable orientation cannot be considered. However, in this study, the visible block surfaces were assumed to be representative of the entire deposit. Furthermore, a certain part of the block surfaces will have come from the previous cliff face. In the present work the cliff face, due to its exposure to external agents before the failure, was recognised as weathered and thus classified as a pre-existent discontinuity.

By involving a combination of spectral, textural and contextual/relational information, the object-based technique comes closer to the way humans interpret information visually from remote sensing data (Laliberte et al., 2004). Before classification, the object-based approach includes image segmentation, that is, the separation of the image in homogeneous groups of contiguous pixels (image objects) with similar radiometric and/or spatial features (Schiewe, 2002; Wyczałek and Wyczałek, 2013). This procedure can be performed in a hierarchical approach, with semantic relationships between objects at different levels, allowing for effective multi-spatial resolution analysis (Taubenböck et al., 2010). The resulting image objects are characterised by several features, such as spectral, shape, textural, hierarchical and contextual information, that can be used for their classification (Bhaskaran et al., 2010).

In the present work, a multi-level object-based approach was developed using the eCognition Developer software, version 9 (Trimble, 2014). The orthophoto of the landslide deposit (68 172 m^2) was subdivided into two different zones (Zone 1 and Zone 2) due to the different light acquisition conditions (Fig. 6). The application of slightly different

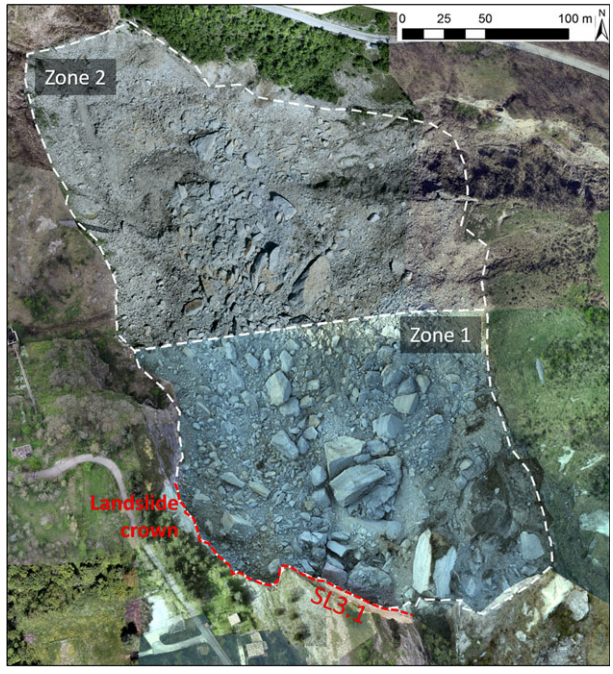

FIG. 6. The orthophoto subdivision. Zone 1 covers 32 707 m^2 and Zone 2 covers 35 465 m^2. The landslide crown is highlighted in red, and it also comprises the SL3.1 discontinuity trace (along which part of the failure took place – see Spreafico et al., 2016).

© 2017 The Authors

thresholds was necessary during the segmentation and classification phases. The object-based approach allows the user to apply locally different strategies for the analysis (Laliberte et al., 2004).

The proposed approach includes two consecutive steps: block identification and classification of their surfaces, between altered and newly formed fractures. The blocks were detected by eliminating the background; in particular, spectral and shape features were used to isolate the background (details of this procedure can be found in Franci and Spreafico, 2016). Image objects were produced by means of the multiresolution segmentation algorithm (Baatz and Schäpe, 2000). Hierarchical segmentation levels were created according to the spatial and spectral characteristics of the elements to be classified, with shape and compactness parameters using a higher scale parameter. The aim was the generation of the "Basic" level, comprising small image objects in order to represent the smallest blocks, and the "Final" level with a significantly increased scale parameter representing bigger blocks. Combining these two levels, the "Optimized" level was obtained, with small image objects in correspondence with small-scale structures and heterogeneous areas, and large objects in homogeneous regions. Block detection was then performed considering image objects at this level.

The classification of the weathered and fresh surfaces was performed on sub-objects, using rules based on spectral information. Rock blocks' classification at the "Optimized" level was transferred to a sub-level characterised by smaller image objects. This allowed the detection of surfaces belonging to different classes, even within the same block (Fig. 7). A rule based on the difference between the R and B bands, in terms of digital number, was applied to distinguish weathered surfaces and fractures of intact rock bridges. Different thresholds were selected for the two parts of the orthophoto:

(1)	Zone 1	$R - B < -40$ fresh $R - B \geq -40$ weathered
(2)	Zone 2	$R - B < -100$ fresh $R - B \geq -100$ weathered.

To evaluate the accuracy of the identification of weathered surfaces and fresh fractures, the classification results were compared with ground-truth data. One hundred points,

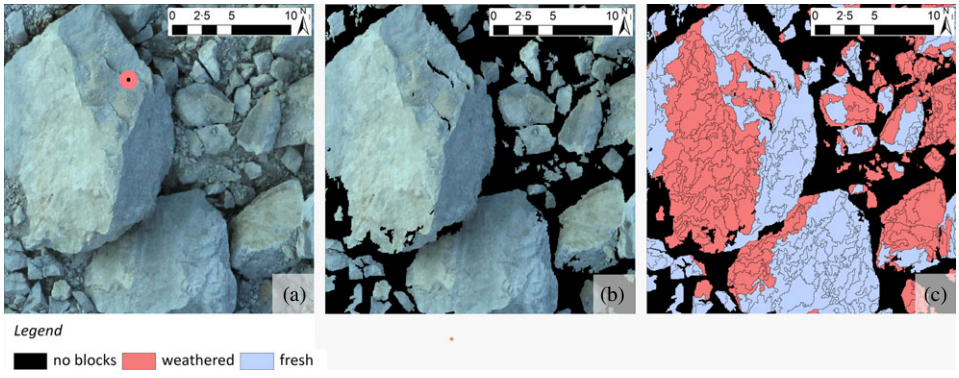

FIG. 7. A subset of the orthophoto. (a) The original data. The red dot represents the point used for the ground truth (weathered surface). The dot has been enlarged for visualisation purposes. (b) Rock blocks identification at the "Optimized" level. (c) Sub-objects representing weathered and fresh surfaces.

© 2017 The Authors

corresponding to 100 pixels, were randomly generated on the orthophoto. Their class, "weathered", "fresh" or "no blocks" (not all the surface area was occupied by blocks), was verified by field surveys on the landslide deposit (Fig. 8). From the comparison, a confusion matrix was compiled; moreover, indexes describing the quality of the classification were derived (Liu et al., 2007). Representing the percentage of correctly classified pixels, the overall accuracy (OA) was calculated by dividing the number of correctly classified check pixels by the total number of available check pixels.

The commission error (CE, meaning a false positive) of a generic class is the percentage of pixels classified into the class of interest which do not belong to that class, according to the ground-truth data (a commission); the omission error (OE, implying a false negative) is the percentage of the pixels, belonging to a specific class in the ground-truth data, which were not classified as such (an omission). From the CE and OE the user accuracy (UA), indicating the probability that a pixel classified on the map represents that category on the ground, and producer accuracy (PA), representing the probability of a reference pixel being correctly classified, were then derived (Congalton, 1991).

Results and Discussion

Results regarding the quantification of intact rock bridges, pre-existing discontinuities and the deposit classification are now presented.

Intact Rock Bridge Quantification

A visual inspection of the TLS point cloud highlighted a similar proportion of the three colours (R, G, B) for all the inspected points classified as fresh rock. In contrast, weathered

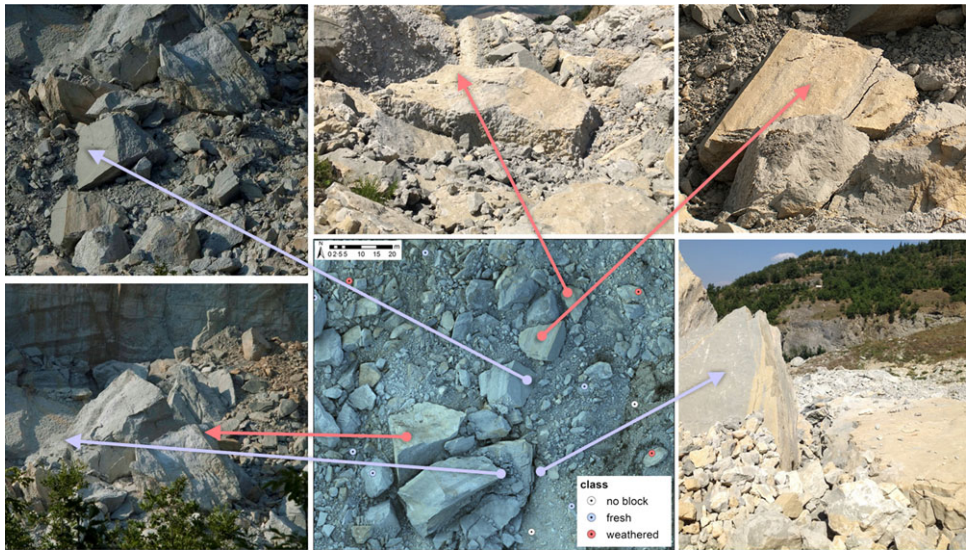

Fig. 8. Example of ground-truth points. The photographs show some of the blocks identified in the field and used as ground truth to validate the classification.

© 2017 The Authors
The Photogrammetric Record © 2017 The Remote Sensing and Photogrammetry Society and John Wiley & Sons Ltd

rock results in the presence of a lower B intensity and a slightly higher R intensity. The results were similar in the UAV point clouds, where the proportion of B was greater than that of the other primary colours for the points identified as fresh rock. Based on this inspection, five colour combinations to be analysed were chosen: R, G, B, R − B and (R + G + B)/3. In Fig. 9, graphs describing the correlation between the colour intensity and the number of points for the fresh and weathered test areas are presented.

With the R and G components, fresh and weathered rock surfaces are hardly differentiable. Only the green component of the UAV point cloud can probably be used for this purpose. The blue component seems to be more suitable for this discrimination. As expected, its intensity is higher on the fresh surfaces. With the R − B combination for the TLS point cloud, freshly exposed rock is represented by a distribution with a mean close to zero, since the three primary colours have a similar intensity. Contrast this with the UAV

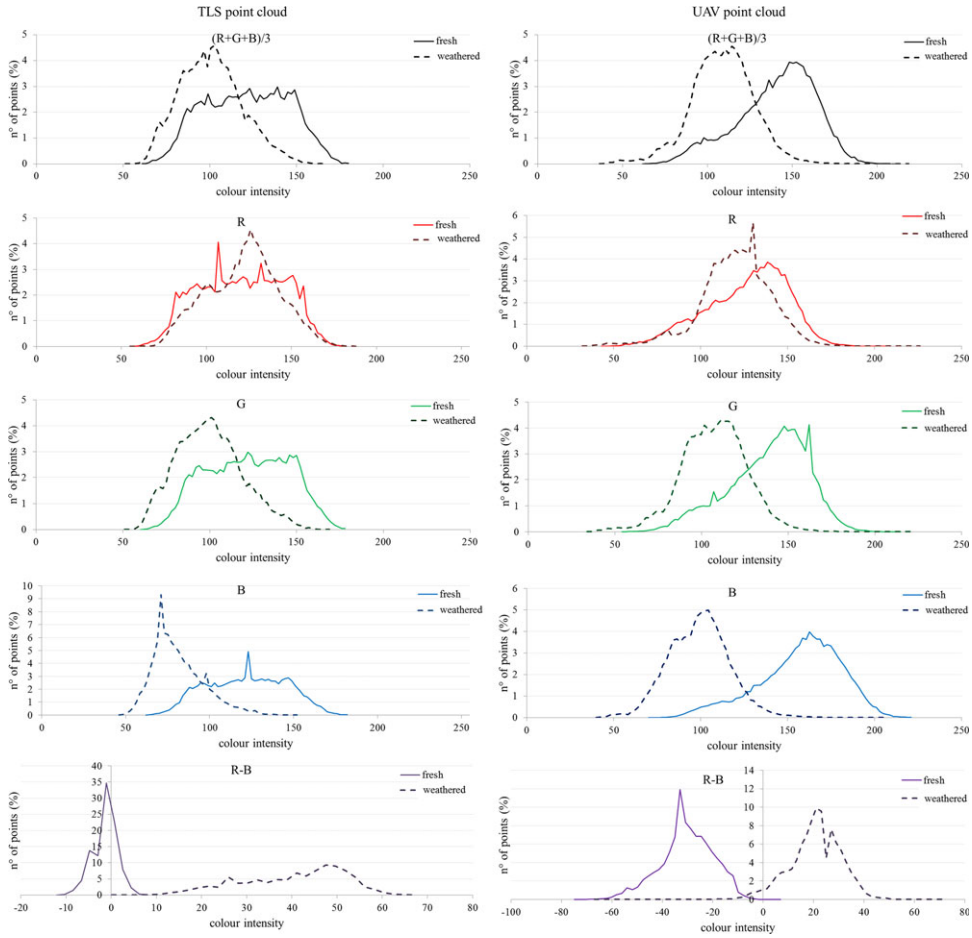

FIG. 9. Colour intensity versus the number of points for fresh and weathered test areas. Left: graphs related to the TLS point cloud. Right: graphs derived from the UAV photogrammetric point cloud. Colour combinations from top to bottom are: (R + G + B)/3; R; G; B; R − B.

© 2017 The Authors

point cloud where, again as expected, the mean of the same distribution is negative due to the higher intensity of the blue colour. Observing these results, the B and R − B intensities can be chosen as the most discriminating between the two classes. In ROC curves (Fig. 10), the diagonal straight line from the bottom-left to the top-right corners, called the *line of no discrimination*, represents a random guess. Curves above this line represent good classifications; the greater the AUC, the higher the model's accuracy. The ROC curves obtained can be used also to select the classification threshold. The different thresholds tested for each combination or colour intensity are, in fact, represented by points on the ROC curves. The best classification is the one closer to the upper left corner of the graph (coordinates (0, 1)), which represents a classification with no false negatives and no false positives. The suitability of the B and R − B intensities was confirmed by the correspondent ROC curves in Fig. 10 and holds true, with different thresholds, for both point clouds. In fact, since a direct comparison between the results was not needed, the colour data was not calibrated.

For both point clouds, the R − B combination proves to be the best prediction method, with an AUC of 0·989 and 0·998 for the TLS and UAV point clouds, respectively. Also, the B intensity can be used, with a slightly lower performance (AUC of 0·952 for the TLS point cloud and of 0·945 for the photogrammetric UAV point cloud). The G intensity has a global accuracy of 0·813 if tested on the TLS point cloud and of 0·839 on the UAV point cloud. Finally, the R intensity showed AUC values below 0·5 (0·394 for the TLS point cloud and 0·435 for the UAV point cloud), which basically indicates no improvements over a random classification. The AUC values provide an idea about the "goodness" of the classifications, but they have to be read with a critical eye. In fact, the ground truth used to calculate the ROC curves, based on visual recognition of weathered rock surfaces, can be slightly biased by certain factors. For example, small pre-existing fractures are difficult to recognise by manual inspection (scale bias). In addition, closed or unconnected pre-existing discontinuities will not be identified because they will not show signs of weathering. Thus, not all the biases present in the classifications were fully highlighted by the analysis of the ROC curves.

Analysing the results in detail, the difference between the B and R − B combination can be explained taking into account that, using only the intensity of one band, the results

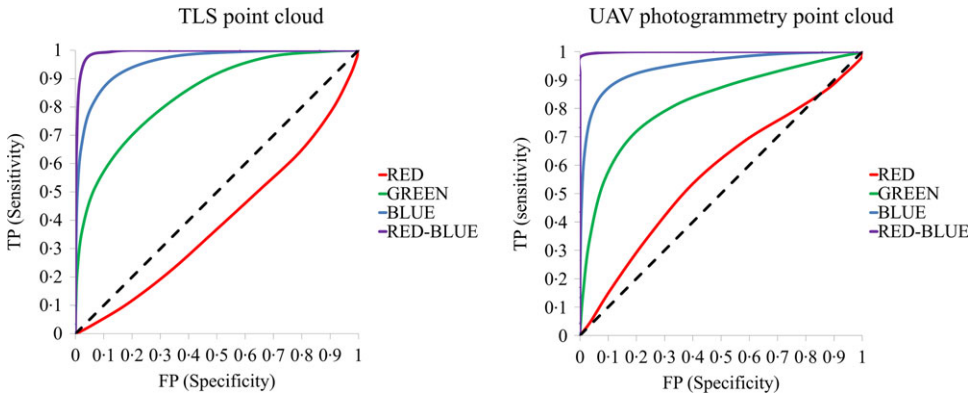

FIG. 10. Comparison of the ROC curves derived for each discrimination method, on the TLS and UAV photogrammetric point clouds. TP = true positives; FP = false negatives.

© 2017 The Authors

are more affected by light conditions and shadows on the cliff, and by the differences in the initial rock colour: shadow areas will result in a lower B intensity for fresh rock as well, and thus can be misinterpreted as weathered surfaces (Fig. 11(b)). By subtracting two colours with R − B, the effect of light conditions is reduced, since a shadowed area will have a lower B intensity but also a lower R intensity (Fig. 11(c)).

The thresholds chosen for the two best classifications (B and R − B) for each of the point clouds are summarised in Table I. The points extracted by applying these thresholds to the subsampled point clouds, and thus identified as fresh rock surfaces, are shown in red in Fig. 12.

Regarding the TLS point cloud, 42% of the points were classified as belonging to fresh surfaces by using the R − B intensity combination, and 45% by analysing only the B intensity. In the UAV photogrammetric point cloud, 53% and 43% of the points were classified as being located on fresh rock surfaces using the R − B and B classifications, respectively. These discrepancies can be explained observing the lower area of the UAV point cloud in Fig. 12(d). This area is located behind the landslide debris, in a sort of trench, meaning it is in shade and thus darker. The darkness of an area can result in errors when dealing with only one colour (B) intensity, while the use of a difference between two colour intensities can minimise the bias. In the TLS, the difference is smaller, because this shaded area was not scanned by the laser, due to topographic obstacles (occlusions).

As regards the pre-existing fractures, they are mainly located in the higher part of the cliff and this is consistent with the failure mechanism interpretation, which considers undermining as the predisposing/triggering factor (Fig. 13). Due to the presence of the landslide deposit, which covers the lower portion of the cliff for about 15 to 30 m, the estimate percentages of intact rock bridges broken during the failure may be slightly underestimated.

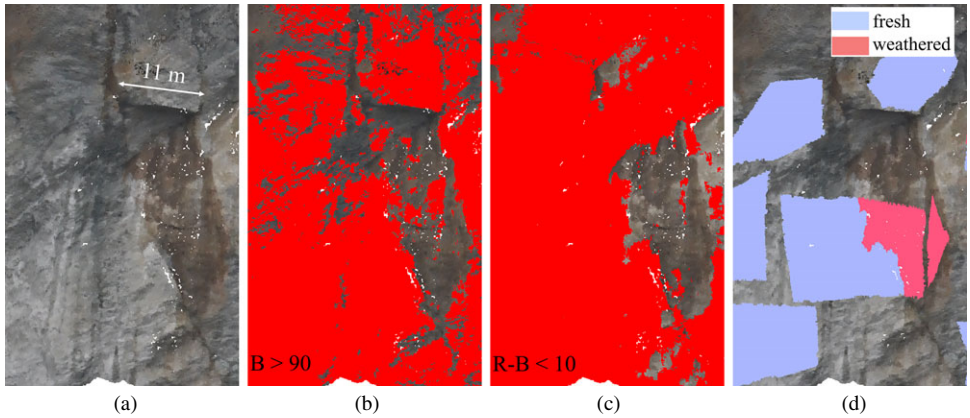

FIG. 11. Details of the TLS point cloud (a) and relative classifications (b) and (c). In red are the points classified as fresh surfaces. (d) Manually classified points, used as a reference to validate the results.

TABLE I. Thresholds chosen to identify fresh rock surfaces on the two point clouds.

Fresh rock	*B*	*R − B*
TLS point cloud	>90	<10
UAV photogrammetric point cloud	>130	<0

© 2017 The Authors

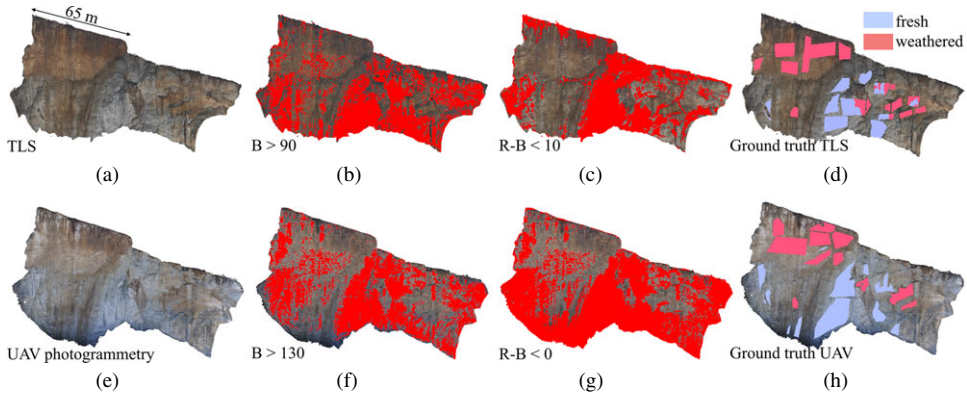

FIG. 12. Subsampled point clouds (a and e) and points extracted applying the thresholds summarised in Table I. The points identified as belonging to fresh rock surfaces are highlighted in red (b, c, f and g). Fresh and weathered surfaces identified through manual mapping were used to validate the results (d and h).

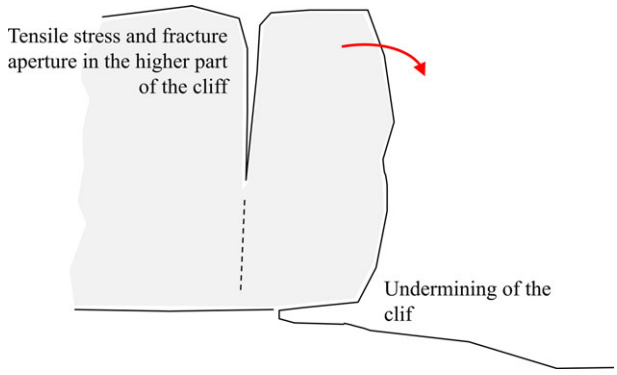

FIG. 13. Simplified sketch of the failure mechanism. Undermining of the cliff is causing tensile stress to develop in the upper portion of the plateau. For this reason, a greater number of open fractures at the top of the cliff are expected.

The pre-existing fractures identified by the procedure, including the surfaces recognised as the pre-existing discontinuity along which part of the failure took place (named SL3.1 in Spreafico et al., 2016), are reported in Fig. 13. Their orientation is consistent with the results of surveys conducted after the failure on the top of the plateau, which identified three main sets of open discontinuities, namely, K1 (89/231), K3 (80/020, including the SL3.1) and K4 (37/061), oriented in the dip/dip direction.

Besides these sets, other non-planar discontinuities in the proximity of the joint SL3.1 showed signs of weathering. The areas, located below the SL3.1, are highlighted in yellow in Fig. 14. In particular, in the lower portion of this area, the staining has an irregular shape and does not cover the entire fracture plane. The most plausible hypothesis for this is that the failure plane was already developing in this area before the rockfall event that occurred on 27th February 2014. The degree of alteration, lower than that on the main SL3.1 surface, is probably an index younger fracture, developed after the joint SL3.1 exhibited a certain

© 2017 The Authors

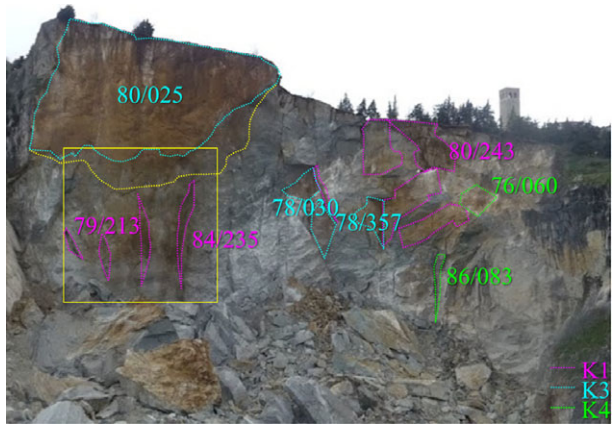

FIG. 14. Main identified pre-existing fractures: the colour is related to the joint set. The areas highlighted in yellow represent an area where weathered surfaces and discontinuity planes do not overlap (for example, only a portion of the joint plane is weathered).

aperture. This highlights how slope damage and fracture propagation are, in fact, time dependent (Kemeny, 2003; Stead and Eberhardt, 2013).

Sturzenegger and Stead (2012) showed that, for large failures, wide rock-surface intervals that resemble intact rock bridges at small scales, if observed in detail, are in fact composed of a low-persistence discontinuity connected by an intact rock fracture. Tuckey (2012) supported this conclusion. The same behaviour, dependent on the resolution of the investigated 3D model, can also be observed in the San Leo cliff (Fig. 15).

Comparison with Numerical Modelling Results

Spreafico et al. (2017) back analysed the same failure using the 2D numerical code Phase2 (version 8 – now called RS2 – see Rocscience Inc., 2014). They used a simplified discrete fracture network (DFN) model to simulate fracture propagation along pre-existing discontinuities together with a Voronoi tessellation for propagation through intact rock masses. Through the DFN definition, it is possible to choose an infinite fracture length, or to specify a persistence (the ratio of the joint length to total length along the joint plane). Different scenarios were simulated, varying the persistence of the pre-existent discontinuities between 25%, 50% and 75%. Despite the differences between the two methods used to estimate the rock bridge percentages, it can be still interesting to make a comparison between the results. This is notwithstanding the fact that with the 2D numerical modelling method only a section was analysed, whereas with the 3D point cloud classification the whole slope was taken into account. Furthermore, different assumptions were made for each of the techniques, both containing intrinsic uncertainties. The failure mechanism was correctly simulated in the numerical model only with a fracture persistence of 50% (Fig. 16). If the pre-existing fractures were assumed to be more persistent (75%), the rock mass behaves as a continuum, not correctly reproducing the shape of the failure surface. On the other hand, with a lower persistence (25%) and thus a higher proportion of intact rock bridges, the slope remained stable even with undermining 10 m deeper than the one measured in the field (about 20 m of undermining). Analysing the simulations' outcomes in more detail, 59% of the resulting failure profile belongs to pre-existing discontinuities, while

© 2017 The Authors

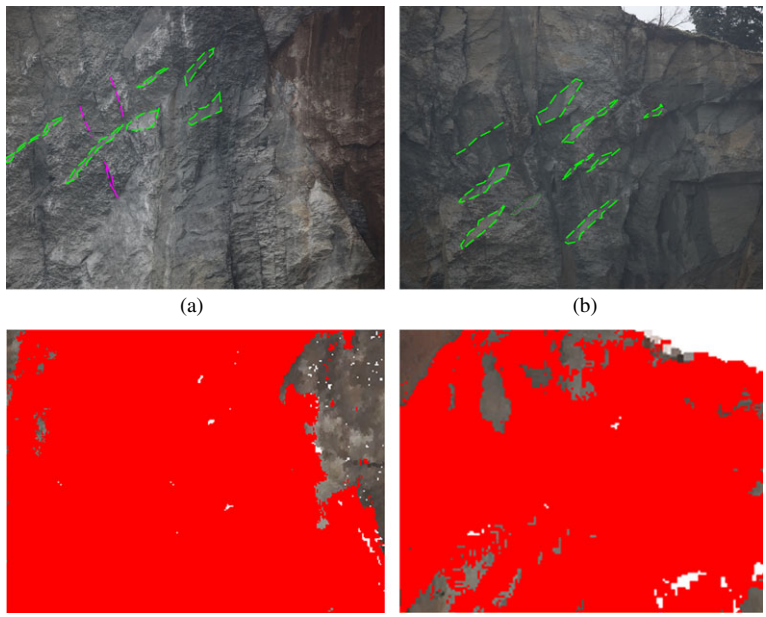

FIG. 15. Details of the cliff showing areas composed of low-persistence discontinuities connected by intact rock. (a, b) Some of the pre-existent fractures are highlighted (set K4 in green, set K1 in magenta). In (c) and (d), fresh surfaces are classified in red using the R − B combination on the TLS point cloud.

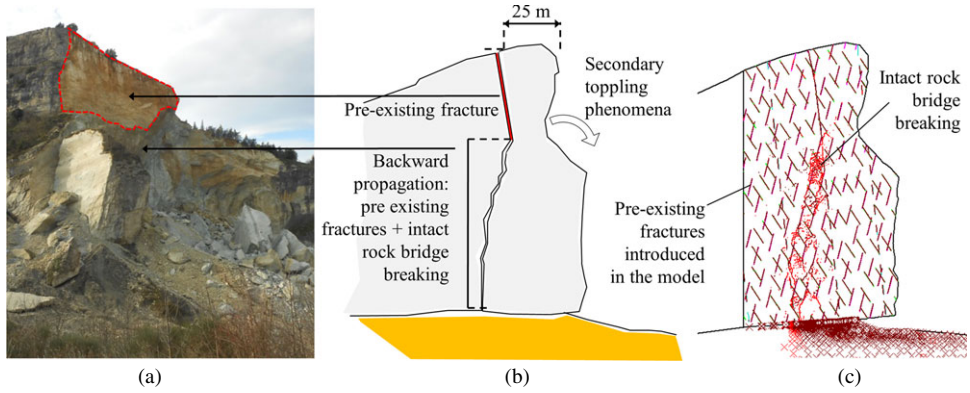

FIG. 16. Numerical modelling workflow. (a) Photograph of the landslide scarp, with the pre-existing discontinuity SL3.1 highlighted in red. (b) Sketch of the 2D section. (c) Modelling results, showing the pre-existing fractures introduced in the model (persistence equal to 50% of the fracture length) and, in red, the intact rock bridge breaking. Modified from Spreafico et al. (2017).

the remaining 41% is due to fracture propagation along intact rock bridges. Since in the numerical models the pre-existing discontinuity SL3.1 was introduced explicitly, to compare the Spreafico et al. (2017) results with the findings of this study the fresh-surface percentages were recalculated removing this discontinuity. Analysing the four classifications

© 2017 The Authors
The Photogrammetric Record © 2017 The Remote Sensing and Photogrammetry Society and John Wiley & Sons Ltd

shown in Fig. 12, the average percentage of fresh fractures appears to be of the order of 54%.

Rock Mass Fragmentation

A detailed example of the block-surface classification obtained by applying the object-based procedure on the deposit orthophoto is shown in Fig. 17. Of the entire deposit (68 172 m^2), 19 018 m^2 was classified as block surfaces. The average size of the detected surfaces was around 10 m^2, with 70% of these surfaces having an area greater than 4 m^2 and the maximum classified block surface having an extent of almost 400 m^2. Thirty-five per cent (6699 m^2) of the block surfaces were recognised as "weathered", while 65% (12 319 m^2) were assigned to the "fresh" surfaces class.

In Table II the results of the accuracy assessment procedure are reported. An overall accuracy of 81% was achieved, proving the effectiveness of the proposed object-based approach in block-surface classification. From the confusion matrix, compiled comparing the classification results with the reference data, some considerations about the errors that affect this procedure were identified. The greater CE value (35·5%) was obtained for the "no blocks" class; it was mainly due to failed or incomplete identification of some boulders. Similar OE values were computed for the "weathered" and "fresh" classes. In general, the confusion between these two classes occurs in shaded areas (for example, a small area of 500 m^2 just below the cliff) that cause anomalous spectral signatures. Moreover, some misclassified pixels were found along the boundaries between the two classes within the same block surface. This can be due to imprecision in the segmentation phase.

About 65% of the block surfaces in the deposit were classified as freshly exposed surfaces. These are composed of both fractures formed during the detachment phase and others caused by the impact with other blocks or with the ground (fragmentation). To gain an idea about the degree of fragmentation, the percentage of fresh fractures on the cliff (about 45% of the cliff surface) and the ones identified in the deposit (about 65% of the block surfaces) can be compared. The differences between these two, besides the discrepancy due to the different methodologies, can be considered as an estimate of the degree of fragmentation.

Examining the blocks in the deposit, this work recognised a high number of blocks in which fragmentation occurred along pre-existing weak rock planes and sedimentary features (for example, bedding planes); examples are shown in Fig. 18. A similar behaviour was

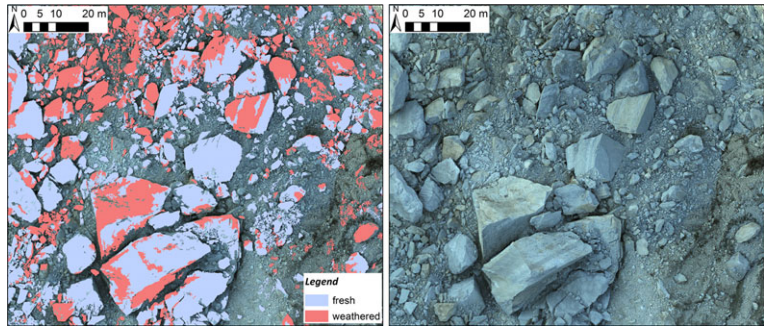

FIG. 17. Left: details of the classification results. Right: original orthophotograph.

© 2017 The Authors

TABLE II. Confusion matrix (left) and accuracy indices (right).

		Ground truth (pixel)				*Accuracy indices (%)*			
		Fresh	*Weathered*	*No blocks*	*Total*	*CE*	*OE*	*UA*	*PA*
Class (pixel)	Fresh	41	4	0	45	8·9	22·6	91·1	77·4
	Weathered	4	20	0	24	16·7	25·9	83·3	74·1
	No blocks	8	3	20	31	35·5	0·0	64·5	100·0
	Total	53	27	20	100	*Overall accuracy* 81%			

CE = commission error; OE = omission error; UA = user accuracy; PA = producer accuracy.

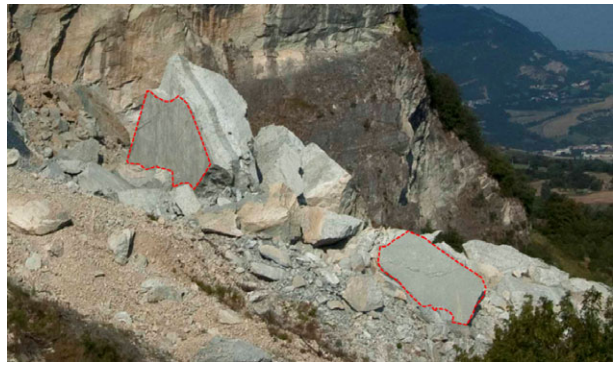

FIG. 18. Photograph depicting examples of blocks in the deposit. Bedding planes along which fragmentation has occurred are highlighted in red.

observed in complex rock failures within similar geological units in the northern Apennines (Ghirotti and Genevois, 2007). As these relatively weak planes were not open or exposed to external agents before the failure, their surfaces are not weathered and they were mapped as planes along which fragmentation occurred.

FINAL REMARKS

Although the importance of intact rock bridges for slope stability has been fully recognised in recent decades, studies on their quantification are very limited and a meaningful database is not yet available. The presented methodology permitted the evaluation of the percentage of fresh and pre-existing discontinuities by analysing a landslide scar immediately after failure. About 40% to 45% of the surface was estimated to be rock bridges. The result is slightly higher than other studies on rock bridge quantification. Paronuzzi and Serafini (2009) recognised a figure of about 26% of intact rock breakage for flexural failure of an overhanging limestone slab (68 m^3). Frayssines and Hantz (2006) mapped the percentage of rock bridges at between 0·2% and 5% for small-scale failures and hypothesised a correlation between the rock bridge percentage and the thickness of the falling slab. Tuckey and Stead (2016), summarising the published literature about estimations of rock bridge content in rock slopes, indicated a range that varied between 0% and 45%.

© 2017 The Authors

The results of the presented procedure can be assumed as an upper threshold for the rock bridge percentage. In fact, as the analysis was based on the spectral information, several factors can contribute to the over-estimation of fresh brittle fractures:

(1) The scale of the 3D model, which influences the ability to distinguish between effective intact rock breakage and a mixture of fresh fractures and low-persistence pre-existing fractures. The resampling of the point cloud to assure a constant point density can thus influence the capability to recognise relatively small features. A good balance between these two requirements should thus be found.
(2) The non-connectivity between pre-existing discontinuities and the flow pathways of fluids. Weathering is a direct consequence of the contact of rock surfaces with air and water. If the fractures are not connected and/or are not included in groundwater pathways, they will not develop signs of weathering and thus will not be identified with the present methodology. This can be useful in hydrogeological frameworks, where attention is focused on connected fractures, but can produce significant overestimation when rock mass stability is the main purpose of the study.

A careful inspection of the original point cloud, of photographic documentation and, when possible, a direct examination of the cliff, in order to identify and take into consideration these biases, is recommended.

As anticipated, by using the presented approach weathered and freshly exposed rock surfaces can be discriminated. A rock bridge that failed a certain length of time before the final collapse (for example, enough time to be subjected to weathering) will thus be recognised as weathered. In this way, only the rock bridges effectively contributing to the stability of the cliff at the time of the final collapse will be considered. In any case, discrimination between pre-existing fractures and pre-failed rock bridges, both recognised as weathered, can be of great interest, for example, to analyse the stress history of the cliff. This can be done by observing the surface texture and non-planarity of the fracture (Tuckey and Stead, 2016). Future development should take into account both the colour and the roughness of the rock surfaces.

The position and orientation of pre-existing fractures can help in the definition or confirmation of the failure mode, and provide some insight regarding the mechanics of the landslide. Where possible, the colour of the discontinuities can also be used to estimate the temporal sequence of fracture propagation; more weathered discontinuities were probably open for a longer time relative to less weathered ones.

The shape of the stained area can also provide some information about the relative age of the fractures, together with groundwater infiltration and flow processes. For example, the shape of the weathered surface in the lower eastern part of the scar, similar to irregular vertical stripes, indicates that water was flowing along the fracture surfaces. A percolation zone was thus recognised, providing some insight into the flow pathways in the rock mass before its failure. However, in such cases it is important to be sure that the change in colour is not due to light changes during the acquisition phases or to other external factors.

Both TLS and UAV photogrammetric data was successfully used for the evaluation of the proportion of pre-existing fractures on the rock cliff. When analysing the point clouds, attention has to be paid to the presence of occlusions. Changes in lighting conditions during the acquisitions have to be avoided, if possible. Elsewhere, different thresholds have to be identified for each of the areas.

The fragmentation occurring after the detachment phase affects the rock-blocks' runout, trajectories (Bowman and Take, 2015) and energy balance (Crosta et al., 2007; Giacomini et al., 2009). Thus, fragmentation should be taken into account in the analysis of failure

© 2017 The Authors

propagation but, due to the complexity of the phenomenon and to the difficulties in its prediction, it is often neglected.

The classification of the landslide deposit, and its comparison with the data extracted from the cliff, provided an indication of the amount of fragmentation that occurred during the 2014 San Leo landslide. Furthermore, observation of the deposit area permitted the recognition of the presence of a consistent number of blocks fragmented along pre-existent weak planes within the rock mass. These observations can be useful to discriminate between the different mechanisms that can be included in the definition of fragmentation, for example, disaggregation along pre-existing discontinuities or the breakage of intact rock.

Different acquisition conditions, within the same orthophoto, can affect the classification results, forcing the user to set different feature thresholds. A further limitation of the use of orthophotos can be recognised in the possibility of mapping only in two dimensions. More accurate results in the boulder-detection phase can be obtained if a digital elevation model (DEM) of the deposit is available. Moreover, only the surface of the deposit can be analysed. If a large percentage of boulders is buried in the deposit, only estimates of the percentage of newly formed fractures can be made. However, in most cases visible blocks can be assumed to be representative of the whole deposit.

Conclusions

During recent decades, remote sensing spatial data has been widely exploited in geoscience. However, the use of the related spectral information is not so common, especially for TLS point clouds. In the present work, the onset and evolution of rock slope instability have been analysed through laser scanner and photogrammetric data. A new approach, based on the analysis of spectral information, has been illustrated. The proposed techniques permitted the evaluation of the percentage of rock bridges and the amount of fracturing occurring after the failure. Is it clear that, despite their importance, these two mechanisms are still far from being completely understood. This is mainly due to the complexity and variability of the processes involved during failure and propagation. An improvement to these topics could emanate from the analysis of different landslide events, in order to compare different situations and reach an understanding about the factors influencing the phenomena at the slope scale.

In this framework, the proposed methodologies can be applied to different cases, helping in data collection. The procedures are semi-automatic, and only an adjustment of the threshold values is required in order to make them applicable to different case studies. Furthermore, the recent advances in the integration of different sensors (Berni et al., 2009; Chen et al., 2010; Gevaert et al., 2015), such as multispectral, hyperspectral, radar or thermal, have raised an increased interest in this kind of data and will permit increasingly sophisticated analyses to be conducted.

Acknowledgements

Suggestions by Federico Cervi were greatly appreciated. The authors wish to thank the Agenzia per la sicurezza territoriale e la protezione civile of the Emilia-Romagna Region (Servizio Area Romagna) for the San Leo orthophoto and the UAV photogrammetric point cloud.

© 2017 The Authors

REFERENCES

BAATZ, M. and SCHÄPE, A., 2000. Multiresolution segmentation: an optimization approach for high quality multi-scale image segmentation. In *Angewandte Geographische Informationsverarbeitung XII* (Eds. J. Strobl, T. Blaschke & G. Griesbner). Wichmann, Karlsruhe, Germany. 264 pages: 12–23.

BECK, J. R. and SHULTZ, E. K., 1986. The use of relative operating characteristic (ROC) curves in test performance evaluation. *Archives of Pathology and Laboratory Medicine*, 110(1): 13–20.

BERNI, J. A. J., ZARCO-TEJADA, P. J., SUAREZ, L. and FERERES, E., 2009. Thermal and narrowband multispectral remote sensing for vegetation monitoring from an unmanned aerial vehicle. *IEEE Transactions on Geoscience and Remote Sensing*, 47(3): 722–738.

BHASKARAN, S., PARAMANANDA, S. and RAMNARAYAN, M., 2010. Per-pixel and object-oriented classification methods for mapping urban features using Ikonos satellite data. *Applied Geography*, 30(4): 650–665.

BOWMAN, E. T. and TAKE, W. A., 2015. The runout of chalk cliff collapses in England and France – case studies and physical model experiments. *Landslides*, 12(2): 225–239.

BURTON, D., DUNLAP, D. B., WOOD, L. J. and FLAIG, P. P., 2011. Lidar intensity as a remote sensor of rock properties. *Journal of Sedimentary Research*, 81(5): 339–347.

CERVI, F., BERTI, M., BORGATTI, L., RONCHETTI, F., MANENTI, F. and CORSINI, A., 2010. Comparing predictive capability of statistical and deterministic methods for landslide susceptibility mapping: a case study in the northern Apennines (Reggio Emilia Province, Italy). *Landslides*, 7(4): 433–444.

CHEN, X., WARNER, T. A. and CAMPAGNA, D. J., 2010. Integrating visible, near-infrared and short-wave infrared hyperspectral and multispectral thermal imagery for geological mapping at Cuprite, Nevada: a rule-based system. *International Journal of Remote Sensing*, 31(7): 1733–1752.

CONGALTON, R. G., 1991. A review of assessing the accuracy of classifications of remotely sensed data. *Remote Sensing of Environment*, 37(1): 35–46.

CROSTA, G. B., FRATTINI, P. and FUSI, N., 2007. Fragmentation in the Val Pola rock avalanche, Italian Alps. *Journal of Geophysical Research*, 112: F01006. 23 pages.

CRUDEN, D. M., 1977. Describing the size of discontinuities. *International Journal of Rock Mechanics and Mining Sciences & Geomechanics Abstracts*, 14(3): 133–137.

EINSTEIN, H. H., VENEZIANO, D., BAECHER, G. B. and O'REILLY, K. J., 1983. The effect of discontinuity persistence on rock slope stability. *International Journal of Rock Mechanics and Mining Sciences & Geomechanics Abstracts*, 20(5): 227–236.

EISENBEISS, H., 2009. *UAV Photogrammetry*. Doctoral thesis, ETH Zürich, Zurich, Switzerland. Dissertation No. 18515. 203 pages.

FISCHER, L., AMANN, F., MOORE, J. R. and HUGGEL, C., 2010. Assessment of periglacial slope stability for the 1988 Tschierva rock avalanche (Piz Morteratsch, Switzerland). *Engineering Geology*, 116(1–2): 32–43.

FRANCESCHI, M., TEZA, G., PRETO, N., PESCI, A., GALGARO, A. and GIRARDI, S., 2009. Discrimination between marls and limestones using intensity data from terrestrial laser scanner. *ISPRS Journal of Photogrammetry and Remote Sensing*, 64(6): 522–528.

FRANCI, F. and SPREAFICO, M. C., 2016. Processing of remote sensing data for the estimation of rock block size distribution in landslide deposits. In *Landslides and Engineered Slopes. Experience, Theory and Practice* (Eds. S. Aversa, L. Cascini, L. Picarelli & C. Scavia). CRC Press, Boca Raton, Florida, USA. 2224 pages: 935–942.

FRAYSSINES, M. and HANTZ, D., 2006. Failure mechanisms and triggering factors in calcareous cliffs of the subalpine ranges (French Alps). *Engineering Geology*, 86(4): 256–270.

GEVAERT, C. M., SUOMALAINEN, J., TANG, J. and KOOISTRA, L., 2015. Generation of spectral–temporal response surfaces by combining multispectral satellite and hyperspectral UAV imagery for precision agriculture applications. *IEEE Journal of Selected Topics in Applied Earth Observations and Remote Sensing*, 8(6): 3140–3146.

GHIROTTI, M. and GENEVOIS, R., 2007. A complex rock slope failure investigated by means of numerical modelling based on laser scanner technique. *Proceedings of the 1st Canada–US Rock Mechanics Symposium* (Eds. E. Eberhardt, D. Stead & T. Morrison). CRC Press, Vancouver, Canada. 1723 pages: 917–924.

GIACOMINI, A., BUZZI, O., RENARD, B. and GIANI, G. P., 2009. Experimental studies on fragmentation of rock falls on impact with rock surfaces. *International Journal of Rock Mechanics and Mining Sciences*, 46(4): 708–715.

GIRARDEAU-MONTAUT, D., 2016. *CloudCompare*. http://www.danielgm.net/cc/ [Accessed: 10th October 2017].

GISCHIG, V., AMANN, F., MOORE, J. R., LOEW, S., EISENBEISS, H. and STEMPFHUBER, W., 2011. Composite rock slope kinematics at the current Randa instability, Switzerland, based on remote sensing and numerical modeling. *Engineering Geology*, 118(1–2): 37–53.

© 2017 The Authors

Hajian-Tilaki, K., 2013. Receiver operating characteristic (ROC) curve analysis for medical diagnostic test evaluation. *Caspian Journal of Internal Medicine*, 4(2): 627–635.

International Society for Rock Mechanics, 1978. Suggested methods for the quantitative description of discontinuities in rock masses. *International Journal of Rock Mechanics and Mining Sciences & Geomechanics Abstracts*, 15(6): 319–368.

Jaboyedoff, M., Oppikofer, T., Abellán, A., Derron, M.-H., Loye, A., Metzger, R. and Pedrazzini, A., 2012. Use of LIDAR in landslide investigations: a review. *Natural Hazards*, 61(1): 5–28.

Kemeny, J., 2003. The time-dependent reduction of sliding cohesion due to rock bridges along discontinuities: a fracture mechanics approach. *Rock Mechanics and Rock Engineering*, 36(1): 27–38.

Kurz, T. H., Dewit, J., Buckley, S. J., Thurmond, J. B., Hunt, D. W. and Swennen, R., 2012. Hyperspectral image analysis of different carbonate lithologies (limestone, karst and hydrothermal dolomites): the Pozalagua Quarry case study (Cantabria, north-west Spain). *Sedimentology*, 59(2): 623–645.

Laliberte, A. S., Rango, A., Havstad, K. M., Paris, J. F., Beck, R. F., McNeely, R. and Gonzalez, A. L., 2004. Object-oriented image analysis for mapping shrub encroachment from 1937 to 2003 in southern New Mexico. *Remote Sensing of Environment*, 93(1–2): 198–210.

Lichti, D. D., 2005. Spectral filtering and classification of terrestrial laser scanner point clouds. *Photogrammetric Record*, 20(111): 218–240.

Liu, C., Frazier, P. and Kumar, L., 2007. Comparative assessment of the measures of thematic classification accuracy. *Remote Sensing of Environment*, 107(4): 606–616.

Paronuzzi, P. and Serafini, W., 2009. Stress state analysis of a collapsed overhanging rock slab: a case study. *Engineering Geology*, 108(1–2): 65–75.

Penasa, L., Franceschi, M., Preto, N., Teza, G. and Polito, V., 2014. Integration of intensity textures and local geometry descriptors from terrestrial laser scanning to map chert in outcrops. *ISPRS Journal of Photogrammetry and Remote Sensing*, 93: 88–97.

Pontius, R. G. and Parmentier, B., 2014. Recommendations for using the relative operating characteristic (ROC). *Landscape Ecology*, 29(3): 367–382.

Rocscience Inc., 2014. Phase2. http://www.rocscience.com [Accessed: 10th October 2017].

Ruiz-Carulla, R., Corominas, J. and Mavrouli, O., 2015. A methodology to obtain the block size distribution of fragmental rockfall deposits. *Landslides*, 12(4): 815–825.

Schiewe, J., 2002. Segmentation of high-resolution remotely sensed data-concepts, applications and problems. *International Archives of Photogrammetry, Remote Sensing and Spatial Information Sciences*, 34(4): 380–385.

Spreafico, M. C., Francioni, M., Cervi, F., Stead, D., Bitelli, G., Ghirotti, M., Girelli, V. A., Lucente, C. C., Tini, M. A. and Borgatti, L., 2016. Back analysis of the 2014 San Leo landslide using combined terrestrial laser scanning and 3D distinct element modelling. *Rock Mechanics and Rock Engineering*, 49(6): 2235–2251.

Spreafico, M. C., Cervi, F., Francioni, M., Stead, D. and Borgatti, L., 2017. An investigation into the development of toppling at the edge of fractured rock plateaux using a numerical modelling approach. *Geomorphology*, 288: 83–98.

Stead, D. and Eberhardt, E., 2013. Understanding the mechanics of large landslides. *Italian Journal of Engineering Geology and Environment*, 6: 85–108.

Sturzenegger, M. and Stead, D., 2009. Close-range terrestrial digital photogrammetry and terrestrial laser scanning for discontinuity characterization on rock cuts. *Engineering Geology*, 106(3–4): 163–182.

Sturzenegger, M. and Stead, D., 2012. The Palliser rockslide, Canadian Rocky Mountains: characterization and modeling of a stepped failure surface. *Geomorphology*, 138(1): 145–161.

Taubenböck, H., Esch, T., Wurm, M., Roth, A. and Dech, S., 2010. Object-based feature extraction using high spatial resolution satellite data of urban areas. *Journal of Spatial Science*, 55(1): 117–132.

Trimble, 2014. *eCognition Developer*. http://www.ecognition.com/suite/ecognition-developer [Accessed: 10th October 2017].

Tuckey, Z. S., 2012. *An Integrated Field Mapping–Numerical Modelling Approach to Characterising Discontinuity Persistence and Intact Rock Bridges in Large Open Pit Slopes*. Master's thesis, Simon Fraser University, Burnaby, British Columbia, Canada. 440 pages.

Tuckey, Z. and Stead, D., 2016. Improvements to field and remote sensing methods for mapping discontinuity persistence and intact rock bridges in rock slopes. *Engineering Geology*, 208: 136–153.

Wyczałek, I. and Wyczałek, E., 2013. Studies on pansharpening and object-based classification of Worldview-2 multispectral image. *Archives of Photogrammetry, Cartography and Remote Sensing*, 23: 109–117.

© 2017 The Authors

Résumé

Dans cette étude, deux processus liés au déclenchement et à l'évolution de grands éboulements ont été analysés au moyen de techniques de modélisation 3D. Dans un premier temps, le nombre de ponts rocheux est estimé en proportion des fractures préexistantes dans un escarpement de glissement de terrain nouvellement formé en analysant l'information spectrale de la masse rocheuse dans des nuages de points générés par balayage laser terrestre et par drone photogrammétrique. La fragmentation de la masse rocheuse après rupture est ensuite évaluée en comparant le pourcentage de fractures nouvellement formées dans l'escarpement et dans le dépôt. À cette fin, une orthophotographie de l'éboulis est traitée par une classification orientée objet. La méthode présentée a permis d'obtenir de nouvelles données sur la rupture de la roche intacte pendant et après la fracturation, et par conséquent d'approfondir les connaissances sur les mécanismes de fracture et de fragmentation des roches.

Zusammenfassung

Die vorgestellte Arbeit behandelt zwei Prozesse in Bezug auf die Entstehung und die Entwicklung großflächiger Felsabstürze mit Hilfe von 3D Modellierungstechniken. Zuerst wurde die Anzahl von Felsbrücken, als ein Maß für vorher vorhandene Risse, in einer neu gebildeten Rutschung eines Steilhangs durch Analyse der spektralen Information der Felsmasse in den Punktwolken aus Terrestrischem Laserscanning (TLS) und unbemannten Flugobjekten (UAV) geschätzt. Als zweites wurde die Aufteilung der Felsmasse nach dem Abbruch durch den Vergleich von neu geformten Rissen im Steilhang und in der Ablagerung bewertet. Dazu wurde ein Orthophoto der Ablagerung mit Hilfe einer objektbasierten Methode klassifiziert. Der beschriebene Prozess ergab neue Daten zu der intakten Felsbruchstelle während und nach dem Abbruch und vertiefte so die Kenntnisse über Felsabstürze und die Mechanismen der Bruchstrukturen.

Resumen

En este trabajo, se han analizado procesos relacionados con el inicio y la evolución de caídas de rocas a gran escala mediante técnicas de modelado 3D. En primer lugar, se ha estimado el número segmentos de roca intacta como proporción de fracturas preexistentes en una escarpa de deslizamiento de tierra recientemente formada mediante el análisis de la información espectral de la masa de roca en las nubes de puntos obtenidas con un escáner láser terrestre (TLS) y vehículos aéreos no tripulados (UAV). En segundo lugar, la fragmentación de la masa de roca después de un deslizamiento se ha evaluado comparando el porcentaje de fracturas recién formadas en la escarpa de deslizamiento y en el depósito. Para este propósito, una ortofotografía del depósito del deslizamiento se clasificó usando un método basado en objetos. El flujo de trabajo presentado obtuvo nuevos datos sobre la rotura de la roca intacta durante y después del deslizamiento y, en consecuencia, profundiza el conocimiento sobre el deslizamiento de la roca y el mecanismo de fragmentación.

摘要

本文应用3D建模技术分析了与大型落石发生和演化的两个过程。首先， 经由分析由地面激光扫描仪 (TLS) 和无人机 (UAV) 获得之点云数据中岩体的光谱信息, 估计新形成的滑坡崖中岩石破裂的数量及其在先前存在的裂缝中的比例。第二， 经由比较岩体中新形成的裂缝与沉积物中的比例， 评估岩体崩坏后的破碎程度。为此， 在滑坡沉积物的正射影像上利用面向对象的方法进行分类。本文所提出的工作流程在岩体破坏期间和之后获得了岩石破裂的新数据, 从而深化了对于岩石破裂和破碎机制的了解。

© 2017 The Authors